Quantifying the migration rate of drainage divides from high-resolution topographic data

Chao Zhou[1], Xibin Tan[2, *], Yiduo Liu[2], Feng Shi[1, 3]

[1] State Key Laboratory of Earthquake Dynamics, Institute of Geology, China Earthquake Administration, Beijing 100029, China

[2] Key Laboratory of Mountain Hazards and Surface Processes, Institute of Mountain Hazards and Environment, Chinese Academy of Sciences, Chengdu 610299, China

[3] Shanxi Taiyuan Continental Rift Dynamics National Observation and Research Station, Beijing 100029, China

*Corresponding author. E-mail address: tanxibin@imde.ac.cn

Abstract

The lateral movement of drainage divides is co-influenced by tectonics, lithology, and climate, and therefore archives a wealth of geologic and climatic information. It also has wide-ranging implications for topography, sedimentary record, and biological evolution, thus has drawn much attention in recent years. Several methods have been proposed to determine the drainage divide's migration state (direction and rate), including geochronological approaches (e.g., ^{10}Be) and topography-based approaches (e.g., χ-plots or Gilbert metrics). A key object in these methods is the channel head, which separates the hillslope and channel. However, due to the limited resolution of topography data, the required channel-head parameters in the calculation often cannot be determined accurately, and empirical values are used in the calculation, which may induce uncertainties. Here, we propose two methods to calculate the migration rate of drainage divides, based on the relatively accurate channel-head parameters derived from high-resolution topographic data. We then apply the methods to an active rift shoulder (Wutai Shan) in the Shanxi rift, and a tectonically stable area (Yingwang Shan) in the Loess Plateau, to illustrate how to calculate drainage-divide migration rates. Our results show that the Wutai Shan drainage divide is migrating northwestward at a rate between 0.21 to 0.27 mm/yr, whereas the migration rates at the Yingwang Shan are approximately zero. This study indicates that the drainage-divide stability can be determined more accurately using high-resolution topographic data. Furthermore, this study takes the cross-divide differences in the uplift rate of channel heads into account in the measurement of drainage-divide migration rate for the first time.

Keywords

Drainage divide; Migration rate; High-resolution topographic data; DEM; Channel head

1. Introduction

The evolution of the Earth's surface is jointly controlled by tectonics, lithology, and climatic conditions (e.g., Molnar and England, 1990; Whipple, 2009; Gallen, 2018; Bernard et al., 2021; Hoskins et al., 2023), providing a basis for reconstructing the past tectonic (Pritchard et al., 2009; Kirby et al., 2012; Shi et al., 2021) or climatic processes (Tucker et al., 1997; Hancock et al., 2002; Schildgen et al., 2022) through topography. The evolution of unglaciated terrestrial terrains is fundamentally coupled with changes in drainage systems through river’s vertical (changes in river long profile) and lateral movements (drainage divide migration and river captures) (Whipple, 2001; Clark et al., 2004; Bonnet, 2009; Willett et al., 2014). Previous studies have extensively investigated how river channel profiles respond to tectonic uplift (Whipple, 2001; Crosby and Whipple, 2006; Kirby et al., 2012), lithological difference (Duvall et al., 2004; Safran et al., 2005; Forte et al., 2016), and precipitation perturbations (Schlunegger et al., 2011; Bookhagen and Strecker, 2012). River's long profiles have been used to study the earthquake events (e.g., Burbank and Anderson, 2001; Wei et al., 2015) and the spatio-temporal variations of uplift (e.g., Whipple et al., 1999; Kirby et al., 2003; Pritchard et al., 2009; Goren et al., 2014). Recent studies show that the widespread lateral movement of river basins driven by geological and/or climatic disturbance (Yang et al., 2019; Zondervan et al., 2020; Zhou et al., 2022a; Bian et al., 2024) also interacts with the adjustment of channel profiles (Willett et al., 2014). Drainage-divide migration, one form of river lateral movement, may not only carry information on geological and/or climatic disturbance (Su et al., 2020; Zondervan et al., 2020; He et al., 2021; Shi et al., 2021; Zhou et al., 2022a; Zeng and Tan, 2023) but also influence the extraction of tectonic information from channel profiles (Goren et al., 2014; Ma et al., 2020; Jiao et al., 2021). Moreover, it has multi-facet consequences for landscape evolution (Scheingross et al., 2020; Stokes et al., 2022), sedimentary processes (Clift & Blusztajn, 2005; Willett et al., 2018; Deng et al., 2020; Zhao et al., 2021), and biological evolution (Waters et al., 2001; Zemlak et al., 2008; Hoorn et al., 2010; Musher et al., 2022). For this reason, the stability of drainage divides has drawn more and more attention in recent years (e.g., Authemayou et al., 2018; Vacherat et al., 2018; Chen et al., 2021; Shelef and Goren, 2021; Sakashita and Endo, 2023; Bian et al., 2024).

Drainage-divide migration is essentially controlled by the cross-divide difference in erosion and topographic slope (Beeson et al., 2017; Dahlquist et al., 2018; Chen et al., 2021; Zhou et al., 2022a). The erosion rates are routinely derived from geochronological techniques, such as cosmogenic nuclides (e.g., ^{10}Be) concentration measurements (Mandal et al., 2015; Struth et al., 2017; Sassolas-Serrayet et al., 2019), which can be used to calculate the migration rates of drainage divides (Beeson et al., 2017; Godard et al., 2019; Hu et al., 2021). However, these techniques are usually based on samples collected from a catchment outlet that is several, or even tens of, kilometers away from the drainage divide and thus may not represent the erosion rates close to the drainage divide (Sassolas-Serrayet et al., 2019; Zhou et al., 2022a). Besides, the high cost of sample processing makes it challenging to determine the drainage divide's motion by measuring the erosion rates throughout the large landscapes. Hence, it would be ideal to find an accessible and efficient method that can be applied to the entire landscape and make full use of the ^{10}Be-derived erosion rates.

The advancement of the digital elevation model (DEM) has promoted the development of geomorphic analysis, making it possible to determine the drainage divide's transient motion through topography analysis. For example, Willett et al. (2014) applied the χ method to map the dynamic state of river basins. Forte and Whipple (2018) proposed the cross-divide comparison of "Gilbert metrics" (including channel heads' relief, slope, and elevation) to determine a drainage divide's migration direction. Others adopted the comparison of slope angle or relief of the hillslopes across a drainage divide to deduce its stability (Scherler and Schwanghart, 2020; Ye et al., 2022; Zhou et al., 2022b). These geomorphic techniques, so far, could only determine the migration direction of drainage divides. Braun (2018) provided an equation that considers both alluvial and fluvial areas to calculate the migration velocity of an escarpment (also a drainage divide). Zhou et al. (2022a) developed a technique to calculate the migration rate through the high base-level χ values on both sides of a drainage divide. These new approaches require channel-head parameters to calculate the migration rate. However, the location of the channel heads sometimes cannot be accurately identified because of the limitation in the resolution of DEMs in natural cases. For this reason, empirical values of channel-head parameters are used in these studies, which may induce uncertainties.

This study aims to establish an approach to derive the migration rate of drainage divides, at a high precision and low cost, based on topographic analysis. We choose a tectonically active area (i.e., the Wutai Shan in the Shanxi Rift) and a tectonically inactive area (i.e., the Yingwang Shan in the Loess Plateau) to demonstrate how to quantify drainage-divide migration rates (Fig. 1). We use the aerial photography acquired by unmanned aerial vehicles (UAVs) and the Structure from Motion (SfM) technology to obtain the high-resolution DEM data of these two areas (0.67 m and 0.84 m spatial resolution in the Wutai Shan and the Yingwang Shan, respectively). Benefiting from the high-resolution data, the location of channel heads can be identified more accurately. We then develop two methods to calculate the drainage-divide migration rates. One is based on the measured channel-head parameters, and the other is based on an improved method of Zhou et al (2022a). Combining with the geological and low-temperature thermochronology studies of the Wutai Shan (Middleton et al., 2017; Clinkscales et al., 2020), we also quantify the cross-divide difference in uplift rates to improve the precision of drainage-divide migration rate.

2. Methods

2.1 Channel-head-point method

According to the detachment-limited stream power model (Howard and Kerby, 1983; Howard, 1994), the channel's erosion rate (*E*) can be expressed as:

$$E = KA^mS^n \tag{1}$$

where *K* is the erosion coefficient, *A* is the upstream drainage area, *S* is the gradient of the river channel, and *m* and *n* are empirical constants.

Because of thresholds such as erosion threshold (the shear stress of overland flow must exceed the threshold of the cohesion of bed material to generate river incision) (Howard and Kerby, 1983; Perron et al., 2008) or landslide threshold (landslides occur when the threshold of soil or rock strength is exceeded in high relief region)

(Burbank et al., 1996; Tucker et al., 1998), river channels (following Eq. 1) emerge at a certain distance from the drainage divide. The region between the channel head and the drainage divide is referred to as the hillslope area, where the erosion is controlled by landslide, collapse, and diffusion processes (Stoke and Dietrich, 2006; Stark, 2010; Braun et al., 2018; Dahlquist et al., 2018). The channel-head point is the highest and the closest point to the drainage divide on a river channel (Clubb et al., 2014). Therefore, the erosion rate at channel-head points (E_{ch}) can be described as:

$$E_{ch} = KA_{cr}^{m}S_{ch}^{n} \tag{2}$$

where E_{ch} is the erosion rate at channel-head points, A_{cr} is the critical upstream drainage area of a channel-head point (Duvall et al., 2004; Wobus et al., 2006), and S_{ch} is the channel-head gradient measured along the channel near the channel-head point. Eq. 2 indicates that the side of a drainage divide with a higher A_{cr} or S_{ch} can have a higher erosion rate than the other side, and is more likely to pirate the opposite drainage basin. Besides, a high erosion coefficient can amplify the drainage basin's erosion rate.

Drainage-divide migration is essentially controlled by the cross-divide difference in erosion rates and topographic slope (Beeson et al., 2017; Dahlquist et al., 2018; Chen et al., 2021; Zhou et al., 2022a; Stokes et al., 2022). Furthermore, the differential uplift should also be considered when using the cross-divide erosion rates at the channel heads to calculate the erosion difference across the divide, especially in the case of tectonic tilting uplift (Zhou et al., 2022a). The drainage-divide migration rate (D_{mr}) can be obtained according to the cross-divide difference in erosion rate and uplift rate and the slopes across the divide (Zhou et al., 2022a):

$$D_{mr} = \frac{\Delta E_{ch} - \Delta U_{ch}}{tan\alpha + tan\beta} \tag{3}$$

where ΔE_{ch} is the difference in erosion rate between the two sides (annotated as α and β) of the drainage divide ($\Delta E_{ch} = E_{ch\alpha} - E_{ch\beta}$). The choice of α or β is arbitrary, and the positive direction of the migration rate is assigned from the α to the β side whereas the negative is the opposite. ΔU_{ch} is the cross-divide difference in uplift rate ($\Delta U_{ch} = U_{ch\alpha} - U_{ch\beta}$), and tanα and tanβ are the gradients on each side of the drainage divide.

Assuming erosion coefficient (K) is the same on both sides of a drainage divide, Eqs. 2 and 3 allow us to derive the equation of drainage divide's migration rate according to the parameters at the channel-head points:

$$D_{mr} = \frac{K\left[\left(A_{cr}^{m} S_{ch}^{n}\right)_{\alpha} - \left(A_{cr}^{m} S_{ch}^{n}\right)_{\beta}\right] - \Delta U_{ch}}{tan\alpha + tan\beta} \tag{4}$$

If the exact value of K is unknown, the drainage divide's unilateral erosion rate can be used as a substitution:

$$D_{mr} = \frac{E_{\alpha}\left[1 - \frac{\left(A_{cr}^{m} S_{ch}^{n}\right)_{\beta}}{\left(A_{cr}^{m} S_{ch}^{n}\right)_{\alpha}}\right] - \Delta U_{ch}}{tan\alpha + tan\beta} \tag{5}$$

or:

$$D_{mr} = \frac{E_{\beta}\left[\frac{\left(A_{cr}^{m} S_{ch}^{n}\right)_{\alpha}}{\left(A_{cr}^{m} S_{ch}^{n}\right)_{\beta}} - 1\right] - \Delta U_{ch}}{tan\alpha + tan\beta} \tag{6}$$

E_{α} and E_{β} are the erosion rates of the α and the β side of the drainage divide, respectively, which can be derived through cosmogenic nuclides (^{10}Be) concentration measurements (Beeson et al., 2017; Godard et al., 2019; Hu et al., 2021). The regional average erosion rate ($\bar{E} = \frac{E_{\alpha} + E_{\beta}}{2}$) can also be used to calculate the migration rate:

$$D_{mr} = \frac{2\bar{E}\left[\frac{\left(A_{cr}^{m}S_{ch}^{n}\right)_{\alpha}-\left(A_{cr}^{m}S_{ch}^{n}\right)_{\beta}}{\left(A_{cr}^{m}S_{ch}^{n}\right)_{\alpha}+\left(A_{cr}^{m}S_{ch}^{n}\right)_{\beta}}\right]-\Delta U_{ch}}{tan\alpha+tan\beta} \tag{7}$$

Based on Eqs. 4-7, the migration rate of drainage divides can be estimated using channel-head parameters combined with one of the erosion-related parameters, erosion coefficient (K), erosion rate at one side of a drainage divide (E_α or E_β), or regional average erosion rate ($\bar{E}$).

2.2 Channel-head-segment method

A channel-head segment is the channel segment just below the channel head (Zhou et al., 2022a). Zhou et al. (2022a) developed a method based on the cross-divide χ contrast of channel-head segments to calculate the migration rate of drainage divides. The essence of the method is the cross-divide comparison of the channel-head segments' normalized channel steepness (k_{sn}) values. k_{sn} is a widely used index (Whipple et al., 1999; Wobus et al., 2006; Hilley and Arrowsmith, 2008; Kirby and Whipple, 2012) that is quantitatively related to E and K ($k_{sn} = \left(\frac{E}{K}\right)^{\frac{1}{n}}$). χ is an integral function ($\chi = \int_{x_b}^{x} \left(\frac{A_0}{A(x)}\right)^{\frac{m}{n}} dx$) of a channel's upstream area (A) to horizontal distance (x) (Royden et al., 2000; Perron and Royden, 2012), and A_0 is an arbitrary scaling area to make the integrand dimensionless.

In the method of Zhou et al. (2022a), the location of channel heads cannot be accurately identified, because it is limited by the resolution of DEM. Therefore, an empirical value of $A_{cr} = 10^5$ m^2 was used in the calculation. Benefiting from the high-resolution DEM in this study, we improve the method in Zhou et al. (2022a) and use the real location of channel heads to calculate the migration rate. When the regional erosion coefficient (*K*) is known and unchanged in the vicinity of the drainage divide, the drainage-divide migration rate can be estimated by the following equation:

$$D_{mr} = \frac{K\left[{k_{sn(\alpha)}}^{n} - {k_{sn(\beta)}}^{n}\right] - \Delta U_{ch}}{tan\alpha + tan\beta} = \frac{K\left\{\left[\frac{(z_{ch}-z_b)_\alpha}{\chi_\alpha}\right]^n - \left[\frac{(z_{ch}-z_b)_\beta}{\chi_\beta}\right]^n\right\} - \Delta U_{ch}}{tan\alpha + tan\beta} \tag{8}$$

where z_{ch} and z_b are the elevations of the channel heads and catchment outlets, respectively. The detailed derivation of Eq. 8 is in Supplementary Materials. The drainage divide's unilateral erosion rate (E_α or E_β) can also be used as a substitution for the *K* value:

$$D_{mr} = \frac{E_\alpha\left\{1 - \left(\frac{\chi_\alpha}{\chi_\beta}\right)^n \left[\frac{(z_{ch}-z_b)_\alpha}{(z_{ch}-z_b)_\beta}\right]^{-n}\right\} - \Delta U_{ch}}{tan\alpha + tan\beta} \tag{9}$$

or:

$$D_{mr} = \frac{E_\beta\left\{\left(\frac{\chi_\alpha}{\chi_\beta}\right)^{-n} \left[\frac{(z_{ch}-z_b)_\alpha}{(z_{ch}-z_b)_\beta}\right]^{n} - 1\right\} - \Delta U_{ch}}{tan\alpha + tan\beta} \tag{10}$$

Alternatively, one can use the regional average erosion rate ($\bar{E}$) to calculate the migration rate:

$$D_{mr} = \frac{2\bar{E}\left\{\frac{\left[\frac{(z_{ch}-z_b)_\alpha}{(z_{ch}-z_b)_\beta}\right]^n - \left(\frac{\chi_\alpha}{\chi_\beta}\right)^n}{\left[\frac{(z_{ch}-z_b)_\alpha}{(z_{ch}-z_b)_\beta}\right]^n + \left(\frac{\chi_\alpha}{\chi_\beta}\right)^n}\right\} - \Delta U_{ch}}{tan\alpha + tan\beta} \tag{11}$$

Based on Eqs. 8-11, the drainage-divide migration rate can be estimated using the χ values of high-base-level channel segments combined with one of the erosion-related parameters, erosion coefficient (*K*), erosion rate at one side of a drainage divide (E_α or E_β), or regional average erosion rate ($\bar{E}$).

We use UAV-acquired aerial photography and structure from motion (SfM) photogrammetry to derive the high-resolution DEM of the two study areas, the Wutai Shan in the Shanxi Rift, and the Yingwang Shan in the Loess Plateau, both located in North China (Fig. 1). The spatial resolution is 0.67 m in the Wutai Shan, and 0.84 m in the Yingwang Shan. Based on the high-resolution topography data, we extract the relevant parameters and calculate the drainage-divide migration rate using the two methods above for each case. Analysis of the data is based on the Matlab toolbox TAK (Forte and Whipple, 2019) and TopoToolbox (Schwanghart and Scherler, 2014).

3. Applications to natural cases

We apply the new methods to two natural examples in North China, the Wutai Shan in the Shanxi Rift and the Yingwang Shan in the Loess Plateau, to demonstrate how to calculate the drainage-divide migration rates (Fig. 1).

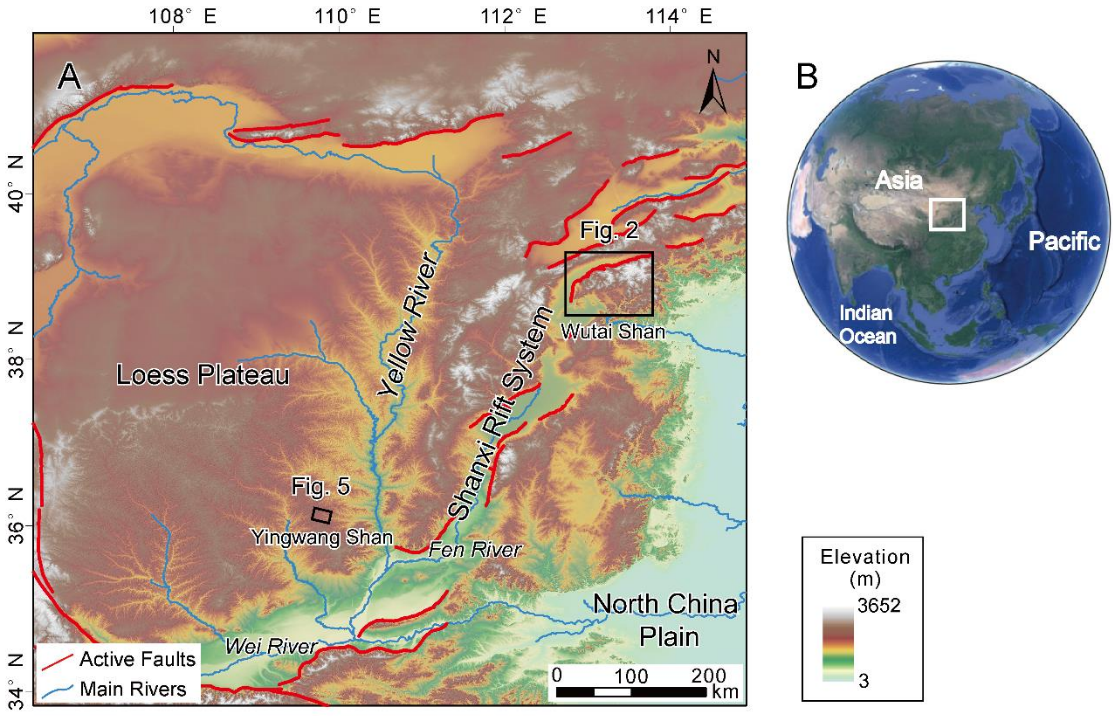

Figure 1. Locations and tectonic background of the two nature cases in North China. The figure is modified from Fig. 7 in Shi et al. (2021). (**A**) Red lines represent the main active faults. Black rectangles show the locations of the two nature cases. Red curve denotes active fault, sourced from https://www.activefault-datacenter.cn/. The topography data (ALOS DEM, 12.5 m resolution) is downloaded from the Alaska Satellite Facility (ASF) Data Search (https://search.asf.alaska.edu/). (**B**) The satellite image downloaded from Google Earth. White rectangles show the location of Panel A.

3.1 Wutai Shan

The Wutai Shan is a tilted fault block on the shoulder of the Shanxi Rift System located in the central North China craton (Fig. 1) (Xu et al., 1993; Su et al., 2021). The tilting uplift of the Wutai Shan is controlled by the Northern Wutai Shan fault, and there is no active fault along the south edge of the Wutai Shan horst (Fig. 2). The bedrock of the Wutai Shan area consists mainly of metamorphic and igneous basement rocks (Clinkscales et al., 2020) and there is no obvious variation in rock erodibility and precipitation in this area (Fig. S2 & S3). Zhou et al. (2022b) reveal that the Wutai Shan drainage divide is migrating northwestward due to the tilting uplift and predicts the drainage divide will move ~10 km to the northwest to achieve a steady state if all geological conditions remain. Geomorphic evidence also exhibits a northwestward migration of the drainage divide (Fig. 3). The plan and satellite views show several barbed tributaries and a captured area around the Wutai Shan drainage divide, which indicate that the tributaries formerly part of the northern drainage have become part of the southern drainage (Fig. 3A&B). The χ-plots analysis shows the southern side of the drainage divide has steeper channels, higher k_{sn}, and lower χ. The χ-plots of paired rivers illustrate obvious characteristics of shrinking-expanding and captured-beheaded rivers (Fig. 3C).

To derive the erosion coefficient of the Wutai Shan area, we calculate the channel steepness (k_{sn}) of this region, assuming $n = 1$ and $m = 0.45$ (Wobus et al., 2006; DiBiase et al., 2010; Perron and Royden, 2012; Wang et al., 2021). We then use the Kriging interpolation method to generate the k_{sn} distribution map (Fig. 2B). In addition, results under the assumptions of m = 0.35 and 0.55, respectively, are shown in Supplementary Materials (Fig. S4). The average k_{sn} value of the upthrown side near the Northern Wutai Shan fault is ~80 $m^{0.9}$ (Fig. 2D). Previous geological study shows that the Quaternary throw rates of the Northern Wutai Shan fault are 0.8-1.6 mm/a (Middleton et al., 2017). The low-temperature thermochronology study shows that the time-averaged long-term throw rates in the late Cenozoic is about 0.25 mm/yr, and there is an accelerated activity in the Wutai Shan area (Clinkscales et al., 2020). According to these studies, we assume a 0.50 ± 0.25 mm/yr uplift/erosion rate in the northern margin of the Wutai Shan (in the footwall of the Northern Wutai Shan fault). Combining with the equation, $K = \frac{E}{{k_{sn}}^{n}}$, and following the approach of previous studies (Kirby and Whipple, 2001; Kirkpatrick et al., 2020; Ma et al., 2020), the erosion coefficient (K) is calculated to be $(6.25 \pm 3.13)\times10^{-6}$ $m^{0.1}yr^{-1}$ in this area.

Because there is no obvious variation in rock erodibility and precipitation in this area (Fig. S2 & S3), we use this value as the erosion coefficient (K) of the Wutai Shan area.

We then apply the two new methods to calculate the migration rate of the drainage divide in the Wutai Shan. We first choose three pairs of rivers (Fig. 4A) and acquire their slope-area plots (Figs. 4B, E, H) and the χ-plots (Figs. 4C, F, I). According to the location of the catchment outlets (Fig. 4A), we obtain the outlet elevations (z_b) from the river's long profiles. According to the breaking point of the slope-area regression line (Duvall et al., 2004) (Figs. 4B, E, H), we obtain the values of the critical upstream drainage area (A_{cr}). According to these values, we separate hillslope and channel areas and mark the position of the channel heads on the χ-plots and the topography map (Fig. 4A). For the χ-plots (Figs. 4C, F, I), we obtain the elevations of channel heads (z_{ch}) and χ values based on the coordinate of the channel-head points. According to the location of the channel heads on the river's long profiles, we calculate the slope of the channel heads' tangent lines, and derive the channel-head gradient (S_{ch}). Topographic gradient (tanα or tanβ) is calculated through the average slope of the hillslope segment near the channel head (Stokes et al., 2022) (not including the hilltop part).

If we assume the rock uplift rate decreases linearly from 0.5 to 0 mm/yr from northwest to southeast of the Wutai Shan horst (~40 km wide), the cross-divide uplift difference in the channel-head points (ΔU_{ch}) (the distance perpendicular to the direction of the boundary fault is ~600 m) is ~0.008 mm/yr. After determining these parameters, we adopt the channel-head-point (Eq. 4) and channel-head-segment (Eq. 8) methods, respectively, to calculate the migration rates. The required data for calculation and the migration rates are shown in Table 1. The calculated results for $m = 0.35$ and 0.55, respectively, are shown in Supplementary Materials (Table S1).

The rivers have different characteristics on both sides of the drainage divide, as illustrated on their slope-area plots (Figs. 4B, E, H) and the χ-plots (Figs. 4C, F, I). For the first site (Fig. 4D), the migration rates calculated by the channel-head-point and channel-head-segment methods are 0.21 mm/yr and 0.26 mm/yr, respectively. For the second site (Fig. 4G), the migration rates are 0.23 mm/yr and 0.27 mm/yr, respectively. For the third site (Fig. 4J), 0.21 mm/yr and 0.22 mm/yr, respectively. The drainage divides of all three points are migrating northwestward, which is consistent with the previous result inferred by the cross-divide contrast of slopes in this area (Zhou et al., 2022b). Furthermore, the migration rates calculated by the two methods are comparable in all three sites.

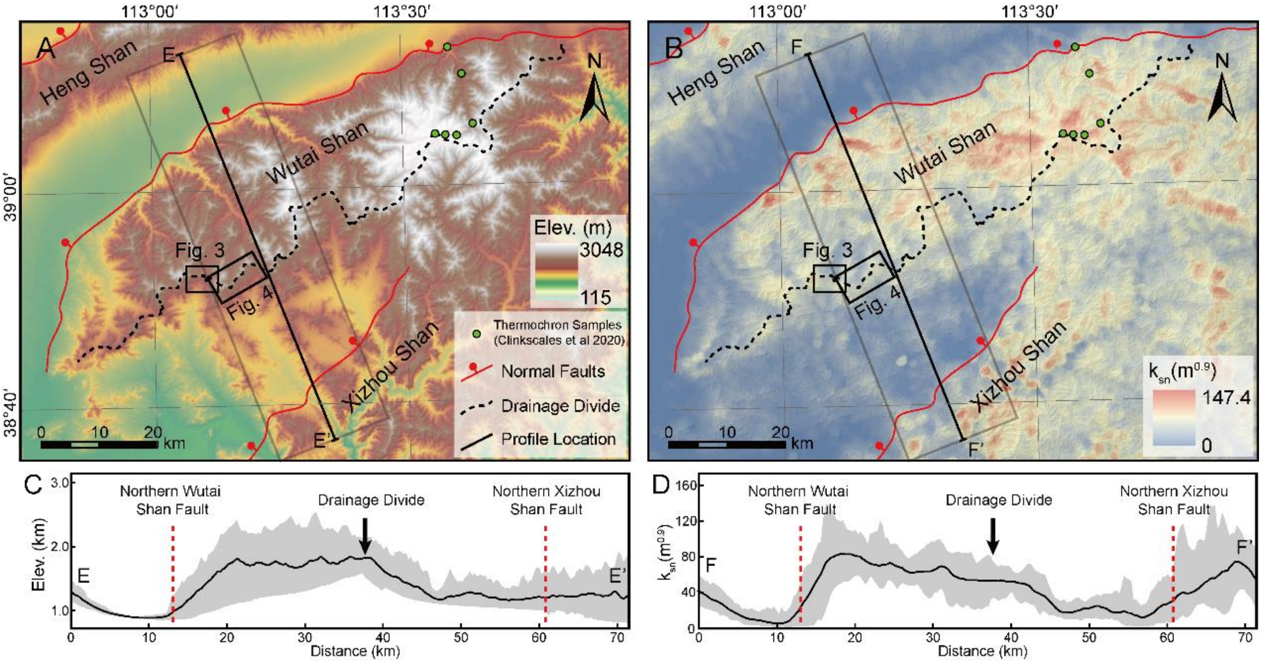

Figure 2. Topography (**A**) and normalized channel steepness (k_{sn}) (**B**) distribution of the Wutai Shan horst and surrounding area in the Shanxi Rift System. The black dashed line shows the location of the main drainage divide. Red lines show the main active faults. The black lines show the location of profiles E-E’ and F-F’. Black rectangles show the area of Fig. 3B & 4A. Gray boxes show the area of the swath profiles in Panels C and D. Green dots denote the locations of the low-temperature thermochronology samples in Clinkscales et al. (2020). The topography data (ALOS DEM, 12.5 m resolution) is downloaded from the Alaska Satellite Facility (ASF) Data Search (https://search.asf.alaska.edu/). The k_{sn} is calculated using TopoToolbox (Schwanghart and Scherler, 2014), and the interpolation uses the Kriging method on ArcGIS. (**C**) Topography swath profile along E-E’. See location in Panel A. (**D**) k_{sn} swath profile along F-F’. See location in Panel B. The swath profiles are extracted using TopoToolbox (Schwanghart and Scherler, 2014). The red dashed lines show the location of the main active normal faults, and the black arrow shows the location of

the main drainage divide. Both swath profiles are 20 km wide (10 km on each side).

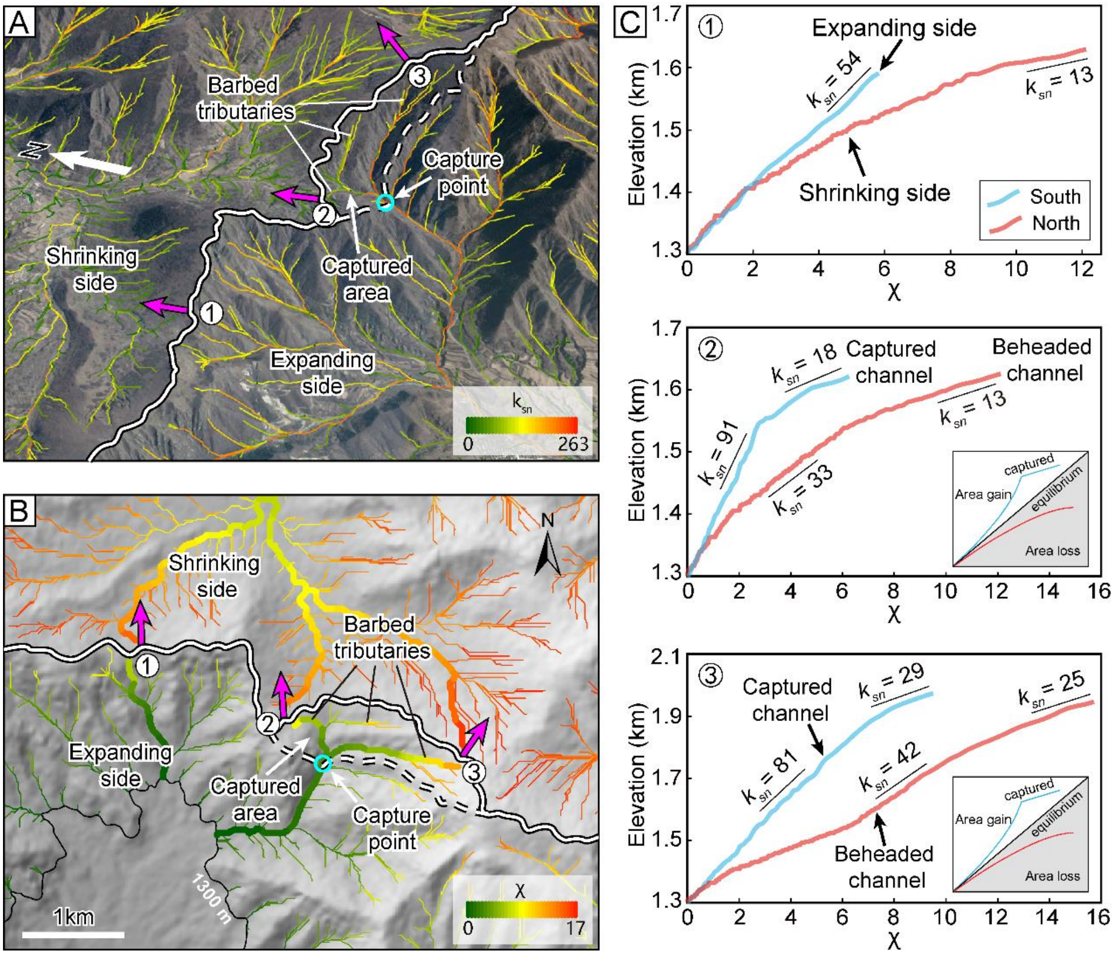

Figure 3. Perspective views and χ map of the drainage divide in the Wutai Shan (see Fig. 2 for location). (A) Perspective views of a captured area and the channels mapped with k_{sn}. The south side of the drainage divide has steeper channels and higher k_{sn} than the north side. Magenta arrows show drainage divide migration directions. The satellite image is from Google Earth. (B) χ map of this area with the outlet elevation of 1300 m. The south side of the drainage divide has lower χ values than the north side. It should be noted that the catchment outlet at the north side of the drainage basins (the 1300 m contour) is out of the map. The χ-plots of the rivers in bold lines are shown in Panel C. The topography data (ALOS DEM, 12.5 m resolution) is

downloaded from the Alaska Satellite Facility (ASF) Data Search (https://search.asf.alaska.edu/). (C) χ-plots of the three paired rivers in Panel B. The blue and red curves correspond to the rivers on the south and north sides, respectively. The χ-plot of River 1 is steeper on the south side, indicating that the river on the south side is expanding and the river on the north side is shrinking. The χ-plots of Rivers 2 and 3 in the captured area show obvious characteristics of the captured and beheaded rivers. The χ-plot is extracted using TAK (Forte and Whipple, 2019) and TopoToolbox (Schwanghart and Scherler, 2014).

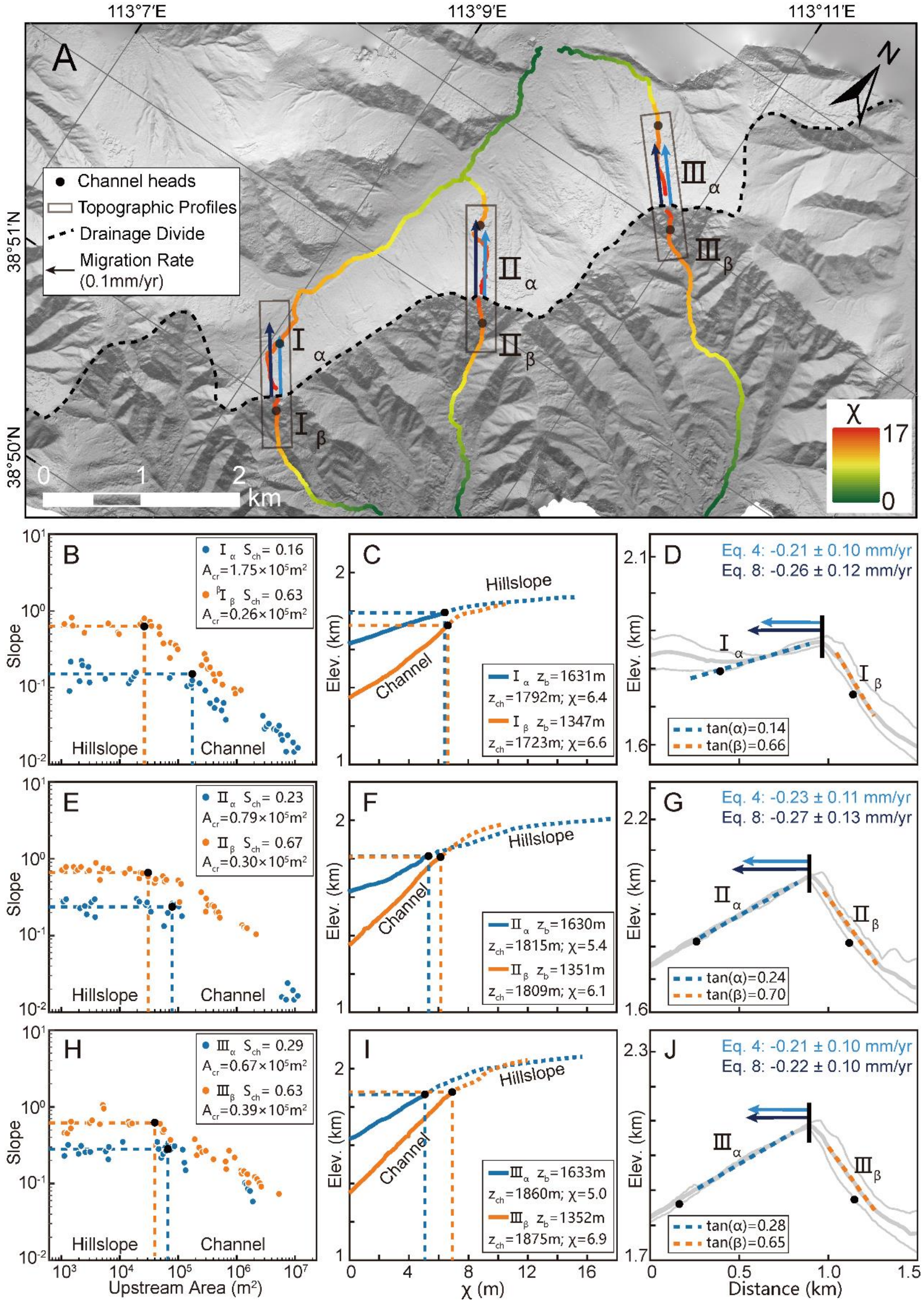

Figure 4. Analytical results of the Wutai Shan drainage divide. (**A**) High-resolution hill-shade map (0.67 m spatial resolution) of the Wutai Shan. The black dashed line shows the location of the main drainage divide. Colored lines show the three pairs of

selected channels used for analysis. The black dots are the channel heads. Black rectangles show the location of the cross-divide topography swath profiles. The black arrows show the direction of drainage-divide migration (**B, E, H**) Slope-area plots of the three pairs of selected channels. The blue and orange dots are the slope-area plots of the north (α) and south (β) sides of the drainage divide respectively. The black dots represent the channel heads. (**C, F, I**) χ-plots of the selected channels. The blue and orange lines are the χ-plots of the north (α) and south (β) sides of the drainage divide respectively. The black dots represent the channel heads. (**D, G, J**) Cross-divide topography swath profiles with the drainage-divide migration rates. The locations of the profiles are in Panel A. The light and dark blue arrows are the drainage-divide migration rates calculated by the channel-head-point (Eq. 4) and channel-head-segment (Eq. 8) methods respectively.

3.2 Yingwang Shan

The Loess Plateau is hosted by the tectonically stable Ordos Block of the North China craton (Yin, 2010; Su et al., 2021). Over the past 2.6 million years, it has accumulated tens to hundreds of meters of eolian sediments (Yan et al., 2014), draping preexisting topography (Xiong et al., 2014). There is no active fault and little to no variation in rock erodibility and precipitation within the area (Shi et al., 2020; Zhou et al., 2022b).

We apply the two methods to Yingwang Shan of Loess Plateau to calculate the drainage-divide migration rate. Similar to the Wutai Shan site, we obtain the slope-area plots (Figs. 5 B, E, H), the χ-plots (Figs. 5 C, F, I), and extract the values of A_{cr}, S_{ch}, z_b, z_{ch}, χ, tanα and tanβ of the rivers. The rate of soil erosion in the study area is about 500 $t \cdot km^{-2} yr^{-1}$ according to the distribution of silt discharge (Fu, 1989). Combining with the assumption of the density of loess, 1.65 $t \cdot m^{-3}$, the present-day erosion rate in the study area is calculated to be 0.3 $mm \cdot yr^{-1}$. Because there is no obvious unequal uplift in this region, we assign that ΔU_{ch} is zero. We also assume $n = 1$ and $m = 0.45$ in the calculation (Wobus et al., 2006; DiBiase et al., 2010; Perron and Royden, 2012; Wang et al., 2021). Then, we use the methods of channel-head parameters (Eq. 7) and channel segments (Eq. 11) to calculate the drainage-divide migration rates. The required data for calculation and the migration rates are shown in Table 1.

All results of the three points show that the drainage-divide migration rate here is close to zero, no matter which method is used in the calculation. The results show that the drainage divide of the study site is in topographical equilibrium, which is consistent with the inference in previous studies (Willett et al., 2014, Zhou et al., 2022b).

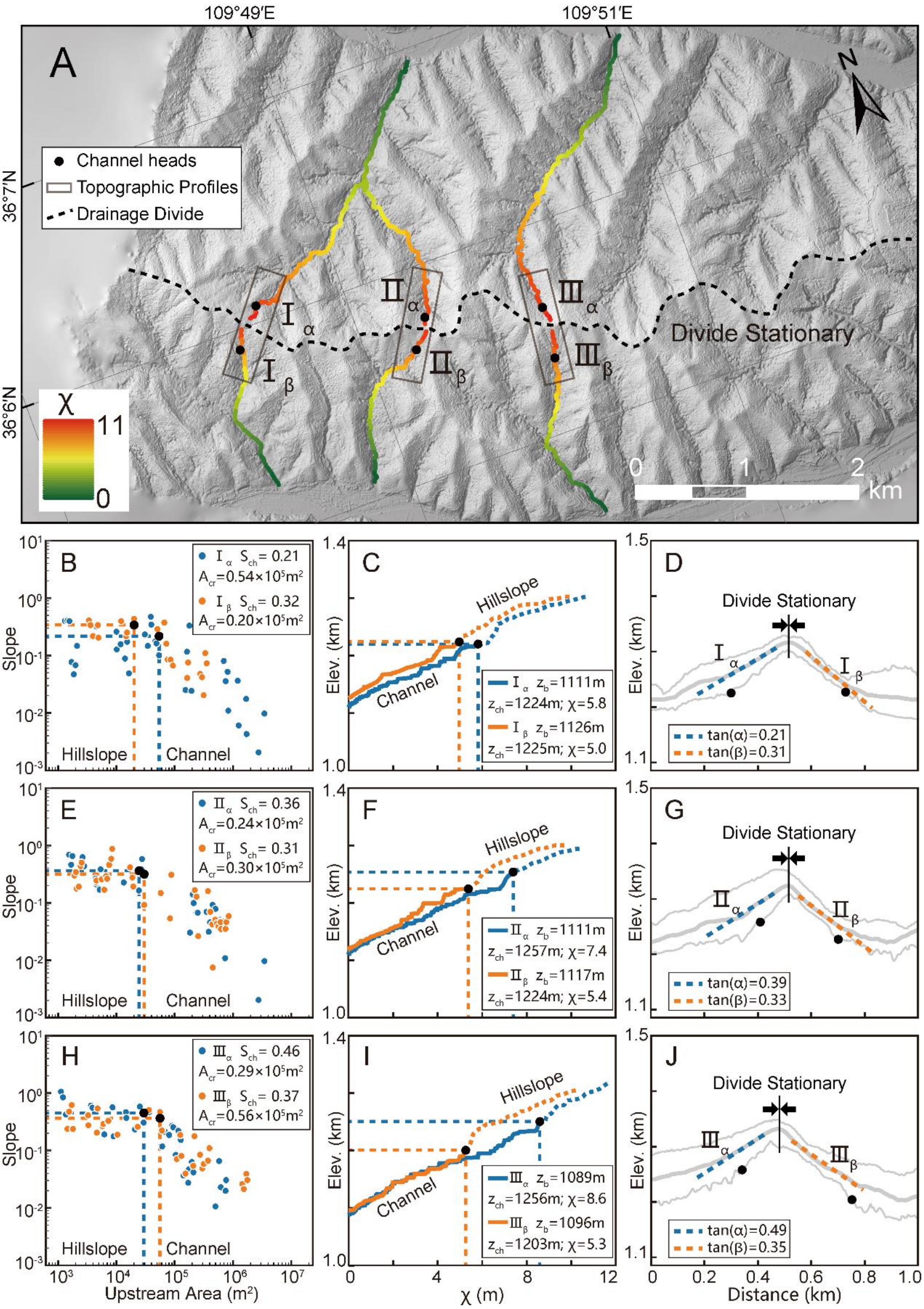

Figure 5. Analytical results of the Yingwang Shan in the Loess Plateau. (**A**) High-resolution hill-shade map (0.84 m spatial resolution). The black dotted line shows the location of the main drainage divide. Colored lines show the three pairs of selected

channels used for analysis. The black dots represent the channel heads. Black rectangles show the location of the cross-divide topography swath profiles. (**B, E, H**) Slope-area plots of the three pairs of selected channels. The blue and orange dots are the data of the north (α) and south (β) sides of the drainage divide respectively. The black dots represent the channel heads. (**C, F, I**) χ-plots of the selected channels. The blue and orange lines are the χ-plots of the north (α) and south (β) sides of the drainage divide respectively. The black dots represent the channel heads. (**D, G, J**) The cross-divide topography swath profiles. The locations of the swath profiles are in Panel A.

Table 1. Channel parameters and migration rates of drainage divides in two field cases.

Natural Cases	No.	A_{cr} (×10^5m^2)	S_{ch}	z_b (m)	z_{ch} (m)	χ	tanα	tanβ	ΔU_{ch} (mm/yr)	D_{mr} (mm/yr) (Channel-head-point method)	D_{mr} (mm/yr) (Channel-head-segment method)
Wutai Shan	Fig. 4 I$_{\alpha}$	1.75	0.16	1631	1792	6.4	0.14	0.66	~ 0.008	-0.21 ±0.10	-0.26 ±0.12
	Fig. 4 I$_{\beta}$	0.26	0.63	1347	1723	6.6					
	Fig. 4 II$_{\alpha}$	0.79	0.23	1630	1815	5.4	0.24	0.70	~ 0.008	-0.23 ±0.11	-0.27 ±0.13
	Fig. 4 II$_{\beta}$	0.30	0.67	1351	1809	6.1					
	Fig. 4 III$_{\alpha}$	0.67	0.29	1633	1860	5.0	0.28	0.65	~ 0.008	-0.21 ±0.10	-0.22 ±0.10
	Fig. 4 III$_{\beta}$	0.39	0.63	1352	1875	6.9					
Yingwang Shan	Fig. 5 I$_{\alpha}$	0.54	0.21	1111	1224	5.8	0.21	0.31	0	~ 0.03	~ -0.01
	Fig. 5 I$_{\beta}$	0.20	0.32	1126	1225	5.0					
	Fig. 5 II$_{\alpha}$	0.24	0.36	1111	1257	7.4	0.39	0.33	0	~ 0.02	~ -0.01
	Fig. 5 II$_{\beta}$	0.30	0.31	1117	1224	5.4					
	Fig. 5 III$_{\alpha}$	0.29	0.46	1089	1256	8.6	0.49	0.35	0	~ 0.02	~ -0.01
	Fig. 5 III$_{\beta}$	0.56	0.37	1096	1203	5.3					

4. Discussion

4.1 Location of channel heads

Willett et al. (2014) pioneered the use of cross-divide χ contrast to gauge the horizontal motion of drainage divides. According to their method, drainage divides are predicted to move toward the side with a higher χ value to achieve geomorphic equilibrium. However, in a region with spatially variable uplift rates, lithology, or precipitation, χ contrast may fail to reflect the drainage-divide migration (Willett et al., 2014; Whipple et al., 2017; Forte and Whipple, 2018; Wu et al., 2022; Zhou and Tan, 2023). In a tectonically active area, the cross-divide χ contrast can only be used in a small area where rock type, precipitation, and uplift rate are nearly uniform (Willett et al., 2014). Combining the advantages of the χ and Gilbert metrics methods, Zhou et al. (2022a) proposed to use the χ contrast with a high base level to calculate the k_{sn} values at the channel heads on both sides of a drainage divide, and quantified the migration rate of drainage divides at the eastern margin of Tibet.

To reduce the cross-divide difference in uplift rate, precipitation, and rock strength, the Gilbert metrics or χ-comparison method in Zhou et al. (2022a) should compare the parameters of points (slope, relief, elevation, and k_{sn}) on both sides of the divide as closely as possible. As the hillslope area (above the channel head) does not follow Eq. 1 (Stoke and Dietrich, 2006; Stark, 2010; Braun et al., 2018; Dahlquist et al., 2018), the channel heads are the closest point to the divide, following Eq. 1. Channel heads, therefore, are suitable for measuring the drainage-divide stability with parameters of the upstream drainage area and channel gradient (Forte and Whipple, 2018; Zhou et al., 2022a). However, limited by the resolution of DEM, the location of the channel heads cannot always be accurately identified. The channel head parameters for calculating the migration rates are usually based on empirical values in previous studies (e.g., A_{cr} = 10^5 m^2 in Zhou et al. (2022a)), which may induce uncertainties.

In this study, we advocate the use of high-resolution DEM to determine a more accurate position and related parameters of the channel head. The use of UAVs to obtain the local DEM has become highly efficient. We advance the theory to calculate the drainage-divide migration rate based on the measured channel-head parameters. With the help of the aerial photography of UAVs and the SfM techniques, it is possible to obtain the high-resolution topography data of drainage divides (Figs. 4A & 5A) and get the required parameters (including the exact locations of the channel heads across the drainage divide) through topography analysis, which could improve the quantitative research on the drainage-divide migration. Furthermore, the method provides a new avenue to combine with catchment-wide ^{10}Be erosion rate or low-temperature thermochronology data to calculate the migration rate, which has great potential for application in places where some variables are hard to be constrained.

4.2 Cross-divide difference in the uplift rate of the channel heads

Although the channel heads across the divide are very close on the spatial scale of an orogenic belt, differential uplift between the channel heads (ΔU_{ch}) could still exist, especially in a tilting horst, such as the Wutai Shan. The cross-divide difference in uplift rate could impact the calculation of the migration rate of drainage divides (Zhou et al., 2022a).

In this study, we quantify the influence of the cross-divide difference in rock uplift rate (ΔU_{ch}) on the calculation of the migration rate of drainage divides at the Wutai Shan, benefiting from the available tectonic and chronological research (Clinkscales et al., 2020) and the newly obtained high-resolution topographic data. In the Wutai Shan horst, ΔU_{ch} across the drainage divide is ~0.008 mm/yr. We estimate the influence of ΔU_{ch} on the drainage-divide migration rate in this case study, which can reduce the error theoretically. If ΔU_{ch} is ignored, the drainage-divide migration rate would decrease by ~4% in the Wutai Shan case. Although ~4% seems to be negligible, such a ratio will increase if the mountain belt is narrower, the tilting uplift is stronger, or the divide is closer to the steady state (i.e., the migration rate is lower) (Whipple et al., 2017; Ye et al., 2022). In other words, the differential uplift may play a significant influence on the measurement of drainage-divide stability in some situations. If we consider an extreme example where the main drainage divide of a tilting mountain range (relatively narrow in width) is at a steady state, the gradient, relief, and elevation of the channel heads (collectively called “Gilbert metrics”) (Forte and Whipple, 2018) will show a systematic cross-divide difference in theory. In this case, the drainage divide would be considered unstable if ΔU_{ch} were neglected. Therefore, this study highlights that ΔU_{ch} should be taken into account, either in a qualitative or a quantitative evaluation of the stability of drainage divides using the parameters on the channel heads.

4.3 Limitations and uncertainties

This study develops the method to calculate the drainage-divide migration rate based on the measured channel-head parameters. However, uncertainties still exist because of the limitations of this technique. First, we assume the erosion coefficient (K) is the same on both sides of a drainage divide in the derivation of the equations. If there are differences in rock erodibility or precipitation across the divide, uncertainties should exist in the results. Second, the calculation of migration rate is based on the erosion rates at the channel area in this study. However, the occurrence of drainage-divide migration is directly driven by the differential erosion of the hillslope area across the divide, mainly via the processes including landslide, collapse, and diffusion (Stoke and Dietrich, 2006; Stark, 2010; Braun et al., 2018; Dahlquist et al., 2018). Such discontinuous processes in the hillslope area make it challenging to constrain erosion rates over such short timescales. Over a relatively longer period (i.e., spanning multiple seismic and climatic cycles), the erosion rate at the channel head area in this study can be comparable with that at the hillslope area (Hurst et al., 2012; Godard et al., 2020).

The accuracy of the data and parameters can also impact the reliability of the results. First, we use the typical values of $n = 1$ and $m/n = 0.45$ in the two natural cases to calculate the migration rate. If the actual values largely deviate from the assumption, errors would be introduced into the results. For this reason, we have added the cases of $m/n = 0.35$ and 0.55 in Supplementary Materials. Further estimation of these values (Mudd et al., 2018) could improve the accuracy of the results. Second, in the case of the Wutai Shan, we refer to the geological and low-temperature thermochronology studies and assume a 0.50±0.25 mm/yr erosion rate at the northern margin of the Wutai Shan (i.e., the footwall of the North Wutai Shan fault). Combining with the present-day k_{sn}, we calculate the erosion coefficient (K) and derive the migration rates of the drainage divide. If the present-day erosion rate deviates from the assumption, errors would be inevitable in the results. Moreover, the horizontal and vertical errors of the DEM data, as well as the calculation errors in slope, upstream area and channel steepness can also affect the reliability of the results. In the case study of the Yingwang Shan, the lush vegetation may bring errors to the DEM data based on the SfM technology. The application of airborne light detection and ranging (LiDAR) technology may help reduce this error. Future studies should take these challenges into account and overcome them.

5. Conclusions

We have developed a new method (called the "channel-head-point method") to calculate the migration rate of drainage divides based on channel-head parameters. We have also improved the previously proposed "channel-head-segment method" (Zhou et al., 2022a) to adapt the theory to areas where the parameters of channel-heads can be accurately determined.

Using the new methods and high-resolution topographic data, we determined the exact locations of the channel heads on both sides of the drainage divide and quantified the drainage-divide migration rates in two natural cases in North China: Wutai Shan in the Shanxi Rift, and Yingwang Shan in the Loess Plateau. The migration rates of the study sites in the Wutai Shan are 0.21-0.27 mm/yr (northwestward). The rates are close to zero in the Yingwang Shan.

Based on the locations of the channel heads and the uplift gradient of the Wutai Shan, we calculated the cross-divide difference in the uplift rate at the channel heads (ΔU_{ch}), which is taken into account in the calculation of the drainage-divide migration rate for the first time. If ΔU_{ch} is overlooked, the drainage-divide migration rate of the study sites in the Wutai Shan will be underestimated by ~4%. Our study highlights that ΔU_{ch} should be considered in the assessment of drainage divide stability based on the cross-divide difference in channel-head parameters.

Data availability. The analysis of data is based on the Matlab toolbox TAK (Forte and Whipple, 2019) and TopoToolbox (Schwanghart and Scherler, 2014). The topography data (ALOS DEM, 12.5 m resolution) is downloaded from the Alaska Satellite Facility (ASF) Data Search (https://search.asf.alaska.edu/).

Acknowledgements. We would like to thank the Editor Simon Mudd, the Reviewer Thomas Bernard, and an anonymous reviewer whose suggestions have greatly improved the paper.

Financial support. This study is supported by the CAS Pioneer Hundred Talents Program (E2K2010010) and the Fundamental Research Funds for the State Key Laboratory of Earthquake Dynamics (LED2021A02).

Competing interests. The authors declare that they have no conflict of interest.

Author contributions. XT and CZ contributed to the design of the research scheme. CZ performed the geomorphic analyses. CZ, XT, and FS carried out field data collection. CZ, XT, YL, and FS contributed to the text and reviewed the paper.

References

Authemayou, C., Brocard, G., Delcaillau, B., Molliex, S., Pedoja, K., Husson, L., et al., 2018. Unraveling the roles of asymmetric uplift, normal faulting and groundwater flow to drainage rearrangement in an emerging karstic landscape. Earth Surface Processes and Landforms, 43(9), 1885-1898. https://doi.org/10.1002/esp.4363

Beeson, H.W., McCoy, S.W., Keen-Zebert, A., 2017. Geometric disequilibrium of river basins produces long-lived transient landscapes. Earth Planet Sc Lett 475, 34-43. https://doi.org/10.1016/j.epsl.2017.07.010

Bernard, T., Sinclair, H.D., Gailleton, B., Fox, M., 2021. Formation of Longitudinal River Valleys and the Fixing of Drainage Divides in Response to Exhumation of Crystalline Basement. Geophys Res Lett 48. https://doi.org/10.1029/2020gl092210.

Bian, S., Tan, X., Liu, Y., Fan, S., Gong, J., Zhou, C., Shi, F., Murphy, M.A., 2024. Orographic rainfall drives the Himalaya drainage divide to move north. Geomorphology, 108952. https://doi.org/10.1016/j.geomorph.2023.108952

Bonnet, S., 2009. Shrinking and splitting of drainage basins in orogenic landscapes from the migration of the main drainage divide. Nature Geoscience 2, 766-771. https://doi.org/10.1038/ngeo666

Bookhagen, B., Strecker, M.R., 2012. Spatiotemporal trends in erosion rates across a pronounced rainfall gradient: Examples from the southern Central Andes. Earth Planet Sc Lett 327-328, 97-110. ttps://doi.org/10.1016/j.epsl.2012.02.005

Braun, J., 2018. A review of numerical modeling studies of passive margin escarpments leading to a new analytical expression for the rate of escarpment migration velocity. Gondwana Research 53, 209-224. https://doi.org/10.1016/j.gr.2017.04.012

Burbank, D.W., Leland, J., Fielding, E., Anderson, R.S., Brozovic, N., Reid, M.R., Duncan, C., 1996. Bedrock incision, rock uplift and threshold hillslopes in the northwestern Himalayas. Nature 379, 505–510. https://doi.org/10.1038/379505a0

Burbank, D.W., Anderson, R.S., 2001. Tectonic Geomorphology. Blackwell Science, Massachusetts p. 274.

Chen, C.-Y., Willett, S.D., Christl, M., Shyu, J.B.H., 2021. Drainage basin dynamics during the transition from early to mature orogeny in Southern Taiwan. Earth Planet Sc Lett 562. https://doi.org/10.1016/j.epsl.2021.116874

Clark, M.K., Schoenbohm, L.M., Royden, L.H., Whipple, K.X., Burchfiel, B.C., Zhang, X., Tang, W., Wang, E., Chen, L., 2004. Surface uplift, tectonics, and erosion of eastern Tibet from large-scale drainage patterns. Tectonics 23, 1-20. https://doi.org/10.1029/2002tc001402

Clift, P.D., Blusztajn, J., 2005. Reorganization of the western Himalayan river system after five million years ago. Nature 438, 1001-1003. https://doi.org/10.1038/nature04379

Clinkscales, C., Kapp, P., Wang, H., 2020. Exhumation history of the north-central Shanxi Rift, North China, revealed by low-temperature thermochronology. Earth Planet Sc Lett 536, 116146. https://doi.org/10.1016/j.epsl.2020.116146

Clubb, F.J., Mudd, S.M., Milodowski, D.T., Hurst, M.D., Slater, L.J., 2014. Objective extraction of channel heads from high-resolution topographic data. Water Resources Research 50, 4283-4304. https://doi.org/10.1002/2013wr015167

Crosby, B.T., Whipple, K.X., 2006. Knickpoint initiation and distribution within fluvial networks: 236 waterfalls in the Waipaoa River, North Island, New Zealand. Geomorphology 82, 16-38. https://doi.org/10.1016/j.geomorph.2005.08.023

Dahlquist, M.P., West, A.J., Li, G., 2018. Landslide-driven drainage divide migration. Geology 46, 403-406. https://doi.org/10.1130/g39916.1

Deng, B., Chew, D., Mark, C., Liu, S., Cogné, N., Jiang, L., O’Sullivan, G., Li, Z., Li, J., 2020. Late Cenozoic drainage reorganization of the paleo-Yangtze river constrained by multi-proxy provenance analysis of the Paleo-lake Xigeda. GSA Bulletin. https://doi.org/10.1130/b35579.1

DiBiase, R.A., Whipple, K.X., Heimsath, A.M., Ouimet, W.B., 2010. Landscape form and millennial erosion rates in the San Gabriel Mountains, CA. Earth Planet Sc Lett 289, 134-144. https://doi.org/10.1016/j.epsl.2009.10.036

Duvall, A., 2004. Tectonic and lithologic controls on bedrock channel profiles and processes in coastal California. J Geophys Res 109. https://doi.org/10.1029/2003jf000086

Forte, A.M., Whipple, K.X., 2018. Criteria and tools for determining drainage divide stability. Earth Planet Sc Lett 493, 102–117. https://doi.org/10.1016/j.epsl.2018.04.026

Forte, A.M., Whipple, K.X., 2019. Short communication: The Topographic Analysis Kit (TAK) for TopoToolbox. Earth Surface Dynamics 7, 87–95. https://doi.org/10.5194/esurf-7-87-2019

Forte, A.M., Yanites, B.J., Whipple, K.X., 2016. Complexities of landscape evolution during incision through layered stratigraphy with contrasts in rock strength. Earth Surface Processes and Landforms 41, 1736-1757. https://doi.org/10.1002/esp.3947

Fu, B., 1989. Soil erosion and its control in the loess plateau of China. Soil Use and Management 5, 76-82. https://doi.org/10.1111/j.1475-2743.1989.tb00765.x

Gallen, S.F., 2018. Lithologic controls on landscape dynamics and aquatic species evolution in post-orogenic mountains. Earth Planet Sc Lett 493, 150-160. https://doi.org/10.1016/j.epsl.2018.04.029

Godard, V., Dosseto, A., Fleury, J., Bellier, O., Siame, L., 2019. Transient landscape dynamics across the Southeastern Australian Escarpment. Earth Planet Sc Lett 506, 397-406. https://doi.org/10.1016/j.epsl.2018.11.017

Godard, V., Hippolyte, J.-C., Cushing, E., Espurt, N., Fleury, J., Bellier, O., Ollivier, V., 2020. Hillslope denudation and morphologic response to a rock uplift gradient. Earth Surface Dynamics 8, 221-243. https://doi.org/10.5194/esurf-8-221-2020

Goren, L., Fox, M., Willett, S.D., 2014. Tectonics from fluvial topography using formal linear inversion: Theory and applications to the Inyo Mountains, California. Journal of Geophysical Research: Earth Surface 119, 1651-1681. https://doi.org/10.1002/2014jf003079

Hancock, G.S., Anderson, R.S., 2002. Numerical modeling of fluvial strath-terrace formation in response to oscillating climate. GSA Bulletin 114, 1131-1142. https://doi.org/10.1130/0016-7606(2002)114<1131:nmofst>2.0.co;2

He, C., Yang, C.J., Turowski, J.M., Rao, G., Roda-Boluda, D.C., Yuan, X.P., 2021. Constraining tectonic uplift and advection from the main drainage divide of a mountain belt. Nat Commun 12, 544. https://doi.org/10.1038/s41467-020-20748-2

Hilley, G.E., Arrowsmith, J.R., 2008. Geomorphic response to uplift along the Dragon's Back pressure ridge, Carrizo Plain, California. Geology 36. https://doi.org/10.1130/g24517a.1

Hoorn, C., Wesselingh, F.P., Steege, H.T., Bermudez, M.A., Antonelli, A., 2010. Amazonia Through Time: Andean Uplift, Climate Change, Landscape Evolution, and Biodiversity. Science 330, 927-931. https://doi.org/10.1126/science.1194585

Hoskins, A.M., Attal, M., Mudd, S.M., Castillo, M., 2023. Topographic Response to Horizontal Advection in Normal Fault-Bound Mountain Ranges. Journal of Geophysical Research: Earth Surface 128. https://doi.org/10.1029/2023jf007126.

Howard, A.D., Dietrich, W.E., Seidl, M.A., 1994. Modeling fluvial erosion on regional to continental scales. Journal of Geophysical Research: Solid Earth 99, 13971-13986. https://doi.org/10.1029/94jb00744

Howard, A.D., Kerby, G., 1983. Channel changes in badlands. Geological Society of America Bulletin 94, 739. https://doi.org/10.1130/0016-7606(1983)94<739:CCIB>2.0.CO;2

Hu, K., Fang, X., Ferrier, K.L., Granger, D.E., Zhao, Z., Ruetenik, G.A., 2021. Covariation of cross-divide differences in denudation rate and χ: Implications for drainage basin reorganization in the Qilian Shan, northeast Tibet. Earth Planet Sc Lett 562, 116812. https://doi.org/10.1016/j.epsl.2021.116812

Hurst, M.D., Mudd, S.M., Walcott, R., Attal, M., Yoo, K., 2012. Using hilltop curvature to derive the spatial distribution of erosion rates. Journal of Geophysical Research: Earth Surface 117, n/a-n/a. https://doi.org/10.1029/2011jf002057

Jiao, R., Fox, M., Yang, R., 2022. Late Cenozoic erosion pattern of the eastern margin of the Sichuan Basin: Implications for the drainage evolution of the Yangtze River. Geomorphology 398, 108025. https://doi.org/10.1016/j.geomorph.2021.108025

Kirby, E., Whipple, K., 2001. Quantifying differential rock-uplift rates via stream profile analysis. Geology 29, 415-418. https://doi.org/10.1130/0091-7613(2001)029<0415:Qdrurv>2.0.Co;2

Kirby, E., Whipple, K., Tang, W., Chen, Z., 2003. Distribution of active rock uplift along the eastern margin of the Tibetan Plateau: Inferences from bedrock channel longitudinal profiles. Journal of Geophysical Research, 108(B4), 2217, https://doi.org/10.1029/2001JB000861.

Kirby, E., Whipple, K.X., 2012. Expression of active tectonics in erosional landscapes. J Struct Geol 44, 54-75. https://doi.org/10.1016/j.jsg.2012.07.009

Kirkpatrick, H.M., Moon, S., Yin, A., Harrison, T.M., 2020. Impact of fault damage on eastern Tibet topography. Geology 48. https://doi.org/10.1130/g48179.1

Ma, Z., Zhang, H., Wang, Y., Tao, Y., Li, X., 2020. Inversion of Dadu River Bedrock Channels for the Late Cenozoic Uplift History of the Eastern Tibetan Plateau. Geophys Res Lett 47. https://doi.org/10.1029/2019gl086882

Mandal, S.K., Lupker, M., Burg, J.-P., Valla, P.G., Haghipour, N., Christl, M., 2015. Spatial variability of 10 Be-derived erosion rates across the southern Peninsular Indian escarpment: A key to landscape evolution across passive margins. Earth Planet Sc Lett 425, 154-167. https://doi.org/10.1016/j.epsl.2015.05.050

Molnar, P., England, P., 1990. Late Cenozoic uplift of mountain ranges and global climate change: chicken or egg? Nature 346, 29-34. https://doi.org/10.1038_346029a0

Mudd, S.M., Clubb, F.J., Gailleton, B., Hurst, M.D., 2018. How concave are river channels? Earth Surface Dynamics 6, 505-523. https://doi.org/10.5194/esurf-6-505-2018

Musher, L.J., Giakoumis, M., Albert, J., Rio, G.D., Rego, M., Thom, G., Aleixo, A., Ribas, C.C., Brumfield, R.T., Smith, B.T., 2021. River network rearrangements promote speciation in lowland Amazonian birds. Cold Spring Harbor Laboratory. https://doi.org/10.1126/sciadv.abn1099

Perron, J.T., Dietrich, W.E., Kirchner, J.W., 2008. Controls on the spacing of first-order valleys. J Geophys Res 113. https://doi.org/10.1029/2007jf000977

Perron, J.T., Royden, L., 2012. An integral approach to bedrock river profile analysis. Earth Surface Processes and Landforms 38, 570-576. https://doi.org/10.1002/esp.3302

Pritchard, D., Roberts, G.G., White, N.J., Richardson, C.N., 2009. Uplift histories from river profiles. Geophys Res Lett 36. https://doi.org/10.1029/2009gl040928

Royden, L., Clark, M., Whipple, K., 2000. Evolution of river elevation profiles by bedrock incision: Analytical solutions for transient river profiles related to changing uplift and precipitation rates. Eos Trans. AGU 81.

Safran, E.B., Bierman, P.R., Aalto, R., Dunne, T., Whipple, K.X., Caffee, M., 2005. Erosion rates driven by channel network incision in the Bolivian Andes. Earth Surface Processes and Landforms 30, 1007-1024. https://doi.org/10.1002/esp.1259

Sassolas-Serrayet, T., Cattin, R., Ferry, M., Godard, V., Simoes, M., 2019. Estimating the disequilibrium in denudation rates due to divide migration at the scale of river basins. Earth Surface Dynamics 7, 1041-1057. https://doi.org/10.5194/esurf-7-1041-2019

Scheingross, J.S., Limaye, A.B., McCoy, S.W., Whittaker, A.C., 2020. The shaping of erosional landscapes by internal dynamics. Nature Reviews Earth & Environment 1, 661-676. https://doi.org/10.1038/s43017-020-0096-0

Scherler, D., Schwanghart, W., 2020. Drainage divide networks – Part 2: Response to perturbations. Earth Surface Dynamics 8, 261-274. https://doi.org/10.5194/esurf-8-261-2020

Schildgen, T.F., van der Beek, P.A., D'Arcy, M., Roda-Boluda, D., Orr, E.N., Wittmann, H., 2022. Quantifying drainage-divide migration from orographic rainfall over geologic timescales: Sierra de Aconquija, southern Central Andes. Earth Planet Sc Lett 579, 117345. https://doi.org/10.1016/j.epsl.2021.117345

Schlunegger, F., Norton, K.P., Zeilinger, G., 2011. Climatic Forcing on Channel Profiles in the Eastern Cordillera of the Coroico Region, Bolivia. The Journal of Geology 119, 97-107. https://doi.org/10.1086/657407

Schwanghart, W., D., S., 2014. Short Communication: TopoToolbox 2 – MATLAB-based software for topographic analysis and modeling in Earth surface sciences. Earth Surface Dynamics 2, 1-7. https://doi.org/10.5194/esurf-2-1-2014

Shelef, E., Goren, L., 2021. The rate and extent of wind-gap migration regulated by tributary confluences and avulsions. Earth Surface Dynamics, 9(4), 687-700. https://doi.org/10.5194/esurf-9-687-2021

Shi, F., Tan, X., Zhou, C., Liu, Y., 2021. Impact of asymmetric uplift on mountain asymmetry: Analytical solution, numerical modeling, and natural examples. Geomorphology 389, 107862. https://doi.org/10.1016/j.geomorph.2021.107862

Shi, W., Dong, S., Hu, J., 2020. Neotectonics around the Ordos Block, North China: A review and new insights. Earth-Science Reviews 200, 102969. https://doi.org/10.1016/j.earscirev.2019.102969

Stark, C.P., 2010. Oscillatory motion of drainage divides. Geophys Res Lett 37. https://doi.org/10.1029/2009gl040851

Stock, J.D., Dietrich, W.E., 2006. Erosion of steepland valleys by debris flows. Geological Society of America Bulletin 118, 1125-1148. https://doi.org/10.1130/b25902.1

Stokes, M.F., Larsen, I.J., Goldberg, S.L., McCoy, S.W., Prince, P.P., Perron, J.T., 2023. The Erosional Signature of Drainage Divide Motion Along the Blue Ridge Escarpment. Journal of Geophysical Research: Earth Surface 128. https://doi.org/10.1029/2022jf006757

Struth, L., Teixell, A., Owen, L.A., Babault, J., 2017. Plateau reduction by drainage divide migration in the Eastern Cordillera of Colombia defined by morphometry and ^{10}Be terrestrial cosmogenic nuclides. Earth Surface Processes and Landforms 42, 1155-1170. https://doi.org/10.1002/esp.4079

Su, P., He, H., Tan, X., Liu, Y., Shi, F., Kirby, E., 2021. Initiation and Evolution of the Shanxi Rift System in North China: Evidence From Low-Temperature Thermochronology in a Plate Reconstruction Framework. Tectonics 40. https://doi.org/10.1029/2020tc006298

Su, Q., Wang, X., Lu, H., Xie, H., 2020. Dynamic Divide Migration as a Response to Asymmetric Uplift: An Example from the Zhongtiao Shan, North China. Remote Sensing 12. https://doi.org/10.3390/rs12244188

Tucker, G.E., Bras, R.L., 1998. Hillslope processes, drainage density, and landscape morphology. Water Resources Research 34, 2751-2764. https://doi.org/10.1029/98wr01474

Tucker, G.E., Slingerland, R., 1997. Drainage basin responses to climate change. Water Resources Research 33, 2031-2047. https://doi.org/10.1029/97wr00409

Vacherat, A., Bonnet, S., Mouthereau, F., 2018. Drainage reorganization and divide migration induced by the excavation of the Ebro basin (NE Spain). Earth Surface Dynamics, 6(2), 369-387. https://doi.org/10.5194/esurf-6-369-2018

Wang, Y., Liu, C., Zheng, D., Zhang, H., Yu, J., Pang, J., Li, C., Hao, Y., 2021. Multistage Exhumation in the Catchment of the Anninghe River in the SE Tibetan Plateau: Insights From Both Detrital Thermochronology and Topographic Analysis. Geophys Res Lett 48. https://doi.org/10.1029/2021gl092587

Waters, J.M., Craw, D., Youngson, J.H., Wallis, G.P., 2001. Genes meet geology: fish phylogeographic pattern reflects ancient, rather than modern, drainage connections. Evolution 55, 1844-1851. https://doi.org/10.1111/j.0014-3820.2001.tb00833.x

Wei, Z., Arrowsmith, J.R., He, H., 2015. Evaluating fluvial terrace riser degradation using LiDAR-derived topography: An example from the northern Tian Shan, China. Journal of Asian Earth Sciences 105, 430-442. https://doi.org/10.1016/j.jseaes.2015.02.016.

Whipple, K.X., 2009. The influence of climate on the tectonic evolution of mountain belts. Nature Geoscience 2, 97-104. https://doi.org/10.1038/ngeo413

Whipple, K.X., Forte, A.M., DiBiase, R.A., Gasparini, N.M., Ouimet, W.B., 2017. Timescales of landscape response to divide migration and drainage capture: Implications for the role of divide mobility in landscape evolution. Journal of Geophysical Research: Earth Surface 122, 248-273. https://doi.org/10.1002/2016JF003973

Whipple, K.X., Kirby, E., Brocklehurst, S.H., 1999. Geomorphic limits to climate-induced increases in topographic relief. Nature 401, 39-43. https://doi.org/10.1038/43375

Willett, S.D., McCoy, S.W., Perron, J.T., Goren, L., Chen, C.Y., 2014. Dynamic reorganization of river basins. Science 343, 1117. https://doi.org/10.1126/science.1248765

Willett, S.D., McCoy, S.W., Beeson, H.W., 2018. Transience of the North American High Plains landscape and its impact on surface water. Nature 561, 528-532. https://doi.org/10.1038/s41586-018-0532-1

Wobus, C., Whipple, K.X., Kirby, E., Snyder, N., Johnson, J., Spyropolou, K., Crosby, B., Sheehan, D., 2006. Tectonics from topography: Procedures, promise, and pitfalls, Tectonics, Climate, and Landscape Evolution, pp. 55-74. https://doi.org/10.1130/2006.2398(04)

Wu, Y., Yang, R., He, C., He, J., 2022. Caution on determining divide migration from cross-divide contrast in χ. Geological Journal 57(12), https://doi.org/10.1002/gj.4530.

Xiong, L.-Y., Tang, G.-A., Li, F.-Y., Yuan, B.-Y., Lu, Z.-C., 2014. Modeling the evolution of loess-covered landforms in the Loess Plateau of China using a DEM of underground bedrock surface. Geomorphology 209, 18-26. https://doi.org/10.1016/j.geomorph.2013.12.009

Xu, X., Ma, X., Deng, Q., 1993. Neotectonic activity along the Shanxi rift system, China. Tectonophysics 219, 305-325. https://doi.org/10.1016/0040-1951(93)90180-R

Yan, M.-J., He, Q.-Y., Yamanaka, N., Du, S., 2014. Location, Geology and Landforms of the Loess Plateau, in: Tsunekawa, A., Liu, G., Yamanaka, N., Du, S. (Eds.), Restoration and development of the degraded Loess Plateau, China. Springer Japan, pp. 3-22. https://doi.org/10.1007/978-4-431-54481-4

Yang, R., Suhail, H.A., Gourbet, L., Willett, S.D., Fellin, M.G., Lin, X., Gong, J., Wei, X., Maden, C., Jiao, R., Chen, H., 2019. Early Pleistocene drainage pattern changes in Eastern Tibet: Constraints from provenance analysis, thermochronometry, and numerical modeling. Earth Planet Sc Lett 531, 1-10. https://doi.org/10.1016/j.epsl.2019.115955

Ye, Y., Tan, X., Zhou, C., 2022. Initial topography matters in drainage divide migration analysis: Insights from numerical simulations and natural examples. Geomorphology 409, 108266. https://doi.org/10.1016/j.geomorph.2022.108266

Yin, A., 2010. Cenozoic tectonic evolution of Asia: A preliminary synthesis. Tectonophysics 488, 293-325. https://doi.org/10.1016/j.tecto.2009.06.002

Zemlak, T.S., Habit, E.M., Walde, S.J., Battini, M.A., Adams, E.D.M., Ruzzante, D.E., 2008. Across the southern Andes on fin: glacial refugia, drainage reversals and a secondary contact zone revealed by the phylogeographical signal of Galaxias platei in Patagonia. Molecular Ecology 17, 5049-5061. https://doi.org/10.1111/j.1365-294X.2008.03987.x

Zeng, X., Tan, X., 2023. Drainage divide migration in response to strike-slip faulting: An example from northern Longmen Shan, eastern Tibet. Tectonophysics 848, 229720. https://doi.org/10.1016/j.tecto.2023.229720

Zhao, X., Zhang, H., Hetzel, R., Kirby, E., Duvall, A.R., Whipple, K.X., Xiong, J., Li, Y., Pang, J., Wang, Y., Wang, P., Liu, K., Ma, P., Zhang, B., Li, X., Zhang, J., Zhang, P., 2021. Existence of a continental-scale river system in eastern Tibet during the late Cretaceous-early Palaeogene. Nat Commun 12, 7231. https://doi.org/10.1038/s41467-021-27587-9

Zhou, C., Tan, X., Liu, Y., Lu, R., Murphy, M.A., He, H., Han, Z., Xu, X., 2022a. Ongoing westward migration of drainage divides in eastern Tibet, quantified from topographic analysis. Geomorphology 402, 108123. https://doi.org/10.1016/j.geomorph.2022.108123

Zhou, C., Tan, X., Liu, Y., Shi, F., 2022b. A cross-divide contrast index (C) for assessing controls on the main drainage divide stability of a mountain belt. Geomorphology 398, 108071. https://doi.org/10.1016/j.geomorph.2021.108071.

Zhou, C., Tan, X., 2023. Quantifying the influence of asymmetric uplift, base level elevation, and erodibility on cross-divide χ difference. Geomorphology 427, 108634. https://doi.org/10.1016/j.geomorph.2023.108634

Zondervan, J.R., Stokes, M., Boulton, S.J., Telfer, M.W., Mather, A.E., 2020. Rock strength and structural controls on fluvial erodibility: Implications for drainage divide mobility in a collisional mountain belt. Earth Planet Sc Lett 538. https://doi.org/10.1016/j.epsl.2020.116221